*J. Fluid Mech.* (1997), *vol.* 339, *pp.* 213–238. Printed in the United Kingdom



# Asymptotic defect boundary layer theory applied to thermochemical non-equilibrium hypersonic flows

By S. SÉROR[1,2], D. E. ZEITOUN[1], J.-PH. BRAZIER[2] AND E. SCHALL[1]

[1]IUSTI-UMR CNRS 139, Department MHEQ, Université de Provence, Technopôle de Château-Gombert, 5 rue Enrico Fermi, 13453 Marseille Cedex 13, France

[2]ONERA CERT Department of Aerothermodynamics, 2, Avenue E. Belin, BP 4025 Toulouse, France

(Received 27 December 1995 and in revised form 23 December 1996)

Viscous flow computations are required to predict the heat flux or the viscous drag on an hypersonic re-entry vehicle. When real gas effects are included, Navier–Stokes computations are very expensive, whereas the use of standard boundary layer approximations does not correctly account for the 'entropy layer swallowing' phenomenon. The purpose of this paper is to present an extension of a new boundary layer theory, called the 'defect approach', to two-dimensional hypersonic flows including chemical and vibrational non-equilibrium phenomena. This method ensures a smooth matching of the boundary layer with the inviscid solution in hypersonic flows with strong entropy gradients. A new set of first-order boundary layer equations has been derived, using a defect formulation in the viscous region together with a matched asymptotic expansions technique. These equations and the associated transport coefficient models as well as thermochemical models have been implemented. The prediction of the flow field around the blunt-cone wind tunnel model *ELECTRE* with non-equilibrium free-stream conditions has been done by solving first the inviscid flow equations and then the first-order defect boundary layer equations. The numerical simulations of the boundary layer flow were performed with catalytic and non-catalytic conditions for the chemistry and the vibrational mode. The comparison with Navier–Stokes computations shows good agreement. The wall heat flux predictions are compared to experimental measurements carried out during the MSTP campaign in the ONERA F4 wind tunnel facility. The defect approach improves the skin friction prediction in comparison with a classical boundary layer computation.

## 1. Introduction

For an inviscid hypersonic flow around a blunt body, under the assumption of a perfect gas, the entropy remains constant along a streamline, except through the bow shock wave, where the entropy jump depends on the local slope of the shock, and thus varies from one streamline to another because of the shock curvature. In the shock layer, an entropy gradient orthogonal to the streamline is thus created. On the rear part of the body, the shock wave tends to be straight and the entropy gradient disappears. The entropy gradient is thus confined to the vicinity of the

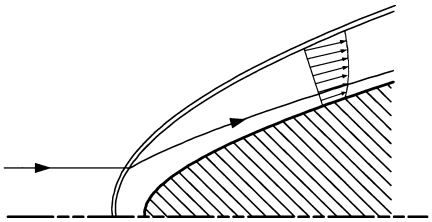

FIGURE 1. Entropy layer on a hypersonic blunt body.

wall in a region called the 'entropy layer'. This layer represents the streamlines which crossed the curved shock wave near the nose. This entropy gradient is related to the vorticity and to the total enthalpy $H_t$ of the flow field through Crocco equation:

$$(\nabla \wedge \boldsymbol{V}) \wedge \boldsymbol{V} = T\,\mathrm{grad}S - \mathrm{grad}H_t.$$

So the streamwise component of the velocity varies through the entropy layer along the normal to the body (figure 1). Since the total enthalpy is constant in the whole flow, the temperature varies too. Therefore this strong shock wave induces an inviscid vortical flow in the shock layer.

Moreover, during an hypersonic re-entry, part of the kinetic energy of the vehicle is transmitted to the flow through the shock wave. As the stagnation enthalpy is conserved, the hypervelocity flow upstream of the shock is transformed into an hyperenthalpy flow downstream of the shock. In this high-enthalpy air flow around the vehicle, the region between the body surface and the detached bow shock is the site of intensive physico-chemical processes. The different internal energy modes (translation, rotation, vibration) of the molecules are far from their equilibrium state; transfers between different modes of energy storage are usually categorized according to the relaxation time associated with each process. The transfer from directed molecular kinetic energy to thermal random translational and rotational energies takes place almost instantaneously through the shock wave, leading to a maximum of the transrotational temperature just behind the shock. Downstream from the shock, this high-temperature gas is in thermal and chemical non-equilibrium, thus the flow relaxes. The return to equilibrium will take place via a redistribution of energy among the internal modes of the molecules and the chemical reactions.

In this paper, only the chemical and vibrational non-equilibrium processes are taken into account for the specific range of Mach numbers investigated. The vibrational mode is thus supplied with energy, and the molecules dissociate. The vibration and chemical relaxation processes proceed together. A reliable computational method for hypersonic viscous flows must include the influence of the vortical inviscid flow on the boundary layer and the real gas effects such as the chemical non-equilibrium and the vibrational relaxation. While Navier–Stokes computations are generally found to be too expensive for design tasks, especially when real gas models are involved, recently some investigations have been made using classical boundary layer codes (see for example Wüthrich & Sawley 1992). Indeed, for large enough Reynolds numbers, the boundary layer is sufficiently small compared to the shock layer to assume that viscous effects are negligible near the shock wave. One can then consider separate calculations for the inviscid shock layer and the viscous boundary layer. Unfortunately, for many hypersonic flows it is not possible to account correctly for the edge conditions within the context of the classical boundary layer method. According to the classical

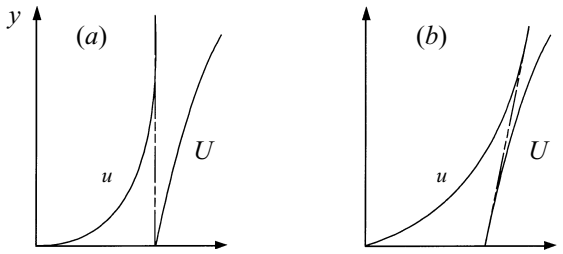


FIGURE 2. Matching scheme at (*a*) first order, (*b*) second order.

boundary layer theory established by Prandtl using an order-of-magnitude analysis, the variables at the edge of the boundary layer are matched with the inviscid variables at the wall (figure 2*a*). This is valid for large Reynolds numbers and thus very thin boundary layers. One can then neglect the evolution of the inviscid flow field throughout the boundary layer. In hypersonic flows, due to the low density of the gas, the Reynolds number is often moderate and the boundary layer thickness becomes no longer negligible compared to the entropy layer thickness. The entropy layer may even be completely 'swallowed' by the boundary layer on the rear part of the body. In such a case, a correct matching cannot be obtained between the inviscid flow and the boundary layer. For that reason Van Dyke (1962) extended this boundary layer theory, using matched asymptotic expansions. This approach is valid when the boundary layer is very thin. Therefore, Van Dyke's second-order theory assumed that the inviscid solution can be represented in the boundary layer by its Taylor expansion at the wall. Consequently, this approach gives a correct matching between the viscous and inviscid solutions only when the inviscid profiles are linear (figure 2*b*). Generally the entropy layer is a region of non-constant vorticity, gradually covered by the boundary layer. Hence, here again neither a correct matching of the viscous and inviscid solutions nor a correct prediction of the influence of the external vorticity on the wall heat flux or the skin friction can be achieved with Van Dyke's approach. To remedy this problem, a defect approach coupled with asymptotic expansions had been proposed by Brazier, Aupoix, & Cousteix (1990), but only perfect gas flow had been considered so far.

This paper presents an extension of this method in the context of hypersonic flows to include real gas effects such as chemical and vibrational relaxation phenomena. The matched asymptotic expansions approach is still used to derive the governing equations since it is a very powerful tool. Only steady two-dimensional planar or axisymmetric laminar compressible reactive flows will be addressed here. An example of application concerns the non-equilibrium flow around the *ELECTRE* model located in the test section of the contoured nozzle of the ONERA high-enthalpy wind tunnel F4. The viscous flow field is studied numerically by solving the defect boundary layer equations using a space marching technique. The influence of the various boundary conditions used for the chemistry and for the vibrational process is clearly pointed out. The results of a comparison with the viscous solution obtained using a full Navier–Stokes code are also presented (see Zeitoun *et al.* 1995). Finally the wall heat flux predictions are compared to experimental measurements and to others computed results from Hachemin & Vérant (1995).

## 2. Basic equations and closure relations

### 2.1. *Air model*

For the stagnation conditions considered, ionization is neglected. Downstream from the shock wave, only dissociation and vibrational relaxation processes are taken into account. Therefore, according to the expected pressure ranges, only atomic oxygen and nitrogen will form, together with nitrogen monoxide. The dissociated air then can be modelled by a mixture of five species, namely $N_2$, $O_2$, NO, N, O. The vibrational relaxation time for nitrogen monoxide being very small in comparison with the flow time scale, this molecule is assumed to be at thermal equilibrium. Thus only the nitrogen and oxygen molecules are taken in vibrational non-equilibrium.

### 2.2. *Flow governing equations and transport properties*

The basic equation set is the Navier–Stokes equations together with relaxation equations for the chemical species and for the vibrational energies. For a steady flow these equations are

$$\begin{aligned}
\text{continuity } & \nabla\cdot(\rho \boldsymbol{V}) = 0,\\
\text{momentum } & \nabla \boldsymbol{V} \otimes \rho \boldsymbol{V} = -\nabla P + \nabla\cdot\boldsymbol{\tau},\\
\text{energy } & \rho \boldsymbol{V}\cdot\nabla h = \boldsymbol{V}\cdot\nabla P + \boldsymbol{\tau} : \nabla \boldsymbol{V} - \nabla\cdot\boldsymbol{\phi},\\
\text{chemical relaxation } & \rho \boldsymbol{V}\cdot\nabla Y_I = \dot{\omega}_I - \nabla\cdot\boldsymbol{Q}_I^D,\\
\text{vibrational relaxation } & \rho \boldsymbol{V}\cdot\nabla\left(Y_J e_{vib,J}\right) = \dot{\Omega}_J - \nabla\cdot\left(e_{vib,J}\boldsymbol{Q}_J^D + \boldsymbol{Q}_{vib,J}\right).
\end{aligned}$$

When the flow is in thermal equilibrium we consider only the first four equations. In these equations, $Y_I$ is the mass fraction of each species, the subscript $I = 1, 2, ..., 5$ represents the five species of the air mixture, $\rho$ is the density of the mixture, $\boldsymbol{V}$ is the velocity vector, $h$ is the enthalpy per unit mass. $P$ is the pressure of the mixture determined from the Dalton law $P = \sum_I P_I$, where $P_I$ is the partial pressure of the $I$-species, assumed to behave as a perfect gas following the relation $P_I = \rho_I (R/M_I)T$ where $M_I$ is the mass per mole of the $I$-species, $\rho_I = \rho Y_I$ being the mass of $I$-species per unit volume and $R$ denotes the universal perfect gas constant. In the vibrational relaxation equations, the subscript $J = 1, 2$ stands respectively for the $N_2$ and $O_2$ molecules in vibrational non-equilibrium. The viscous stress tensor $\boldsymbol{\tau}$ under the Stokes assumption is

$$\boldsymbol{\tau} = \mu\left(\nabla \boldsymbol{V} + {}^t\nabla \boldsymbol{V}\right) - \tfrac{2}{3}\mu(\nabla\cdot\boldsymbol{V})\,\mathbf{1}.$$

The mass diffusion for the $I$-species reads

$$\boldsymbol{Q}_I^D = \rho Y_I \boldsymbol{V}_I^D$$

with $\boldsymbol{V}_I^D$ the diffusion velocity for the $I$-species. As a first step, diffusion fluxes are approximated by the Fick law, with a single diffusion coefficient calculated assuming a constant Lewis number. Therefore the diffusion flux is

$$\boldsymbol{Q}_I^D = -\rho D \nabla Y_I$$

This approximation avoids having to compute all the binary diffusion coefficients involved in the general expression for the diffusion flux which stems from the kinetic theory of gases as given in Hirschfelder, Curtiss, & Bird (1954). The heat flux expression is

$$\boldsymbol{\phi} = \boldsymbol{\phi}_{trans,rot} + \boldsymbol{\phi}_{vib} + \boldsymbol{\phi}_{chem}$$

with

$$\boldsymbol{\phi}_{trans,rot} = -\lambda_{trans,rot}\nabla T,$$

$$\boldsymbol{\phi}_{vib} = \sum_{k=molecules} \boldsymbol{Q}_{vib,k},$$

whereh

$$\boldsymbol{Q}_{vib,k} = -\lambda_{vib,k}\nabla T_{vib,k}$$

is the vibrational heat flux of the $I$-species and

$$\boldsymbol{\phi}_{chem} = \sum_{I} h_I \boldsymbol{Q}^D_{vib,I}.$$

$\boldsymbol{\phi}_{trans,rot}$, $\boldsymbol{\phi}_{vib}$, $\boldsymbol{\phi}_{chem}$ represent the energy fluxes due to the transport of translation/rotation energy, to the transport of vibration energy of the molecular species and to the transport of the various species with their own enthalpy respectively. The viscosity of pure species is given by the kinetic theory of gases in Hirschfelder *et al.* (1954), and the Wilke approximate mixture rule is used (see Wilke 1950). The translation/rotation thermal conductivity of a pure species is deduced from its viscosity with the help of the Eucken relation. Here again the Wilke mixture rule is used to compute the translation/rotation mixture conductivity. The viscosity and the translation/rotation conductivity have been computed using the collision integral method from Hirschfelder *et al.* (1954), with the Lennard–Jones potential. The values of the potential wells and the collision diameters have been taken from Glotz & Schönauer (1977). The collision integrals are computed with the help of the Hattikudur & Thodos (1970) formula. The vibrational thermal conductivities of the molecules are expressed in terms of the single diffusion coefficient as recommended by Pascal & Brun (1993).

### 2.3. *Chemical model*

The chemical model to describe the gas dissociation consists of seventeen reactions for the above five-species mixture. Each molecule may dissociate by collision with any of the five species and nitrogen monoxide can be formed and destroyed by the exchange reactions. The chemical reaction set is

dissociation reactions

$$\mathrm{N_2 + M \rightleftharpoons N + N + M},$$
$$\mathrm{O_2 + M \rightleftharpoons O + O + M},$$
$$\mathrm{NO + M \rightleftharpoons N + O + M};$$

exchange reactions

$$\mathrm{NO + O \rightleftharpoons N + O_2},$$
$$\mathrm{O + N_2 \rightleftharpoons N + NO},$$

where $M$ stands for any of the five species. The forward reaction rates $K_{f,r}$, for the $r^{\mathrm{th}}$ reaction, depend on the temperature and are computed from a modified Arrhenius equation,

$$K_{f,r} = A_r T^{\alpha_r} \exp\left(\frac{-\theta_r}{T}\right)$$

where the constants $A_r$, $\alpha_r$ and $\theta_r$ can be found in Gardiner (1984). The backward reaction rates $K_{b,r}$ are obtained from the equilibrium constant, given by classical thermodynamic (see for example Barrère & Prudhomme 1973) and calculated from

the thermodynamic variables of the mixture. If we use the general Penner notation for the $r$-reaction

$$\sum_I \nu'_{I,r} A_I \rightleftharpoons \sum_I \nu''_{I,r} A_I$$

then the variation of the mole number $n_I = \rho_I / M_I$ for the $I$-species due to the chemical reactions is

$$\left(\frac{\mathrm{d}n_I}{\mathrm{d}t}\right)_{chem} = \sum_{r=1}^{17} \left(\nu''_{I,r} - \nu'_{I,r}\right) \left(K_{f,r} \prod_J n_J^{\nu'_{J,r}} - K_{b,r} \prod_J n_J^{\nu''_{J,r}}\right)$$

and the mass production rate is

$$\dot{\omega}_I = M_I \left(\frac{\mathrm{d}n_I}{\mathrm{d}t}\right)_{chem}.$$

### 2.4. *Vibrational relaxation model*

The production term which appears in the vibrational relaxation equation is a combination of chemical production and vibrational relaxation rates

$$\dot{\Omega}_J = e_{vib,J} \dot{\omega}_J + \rho Y_J \dot{\omega}_{vib,J}.$$

We consider only the vibrational energy exchanges that occur through V-T processes i.e. energy exchanges between the translational and vibrational modes, as described in Landau & Teller (1936). Following their results, the vibrational source term can be written as

$$\dot{\omega}_{vib,J} = \left(\dot{\omega}_{vib,J}\right)_{V-T} = \frac{\bar{e}_{vib,J}(T) - e_{vib,J}\left(T_{vib,J}\right)}{\tau_J^{VT}}$$

where $e_{vib,J}\left(T_{vib,J}\right)$ is the actual vibrational energy and $\bar{e}_{vib,J}(T)$ is the vibrational energy of the molecule if it were in vibrational equilibrium with the translation temperature $T$. The relaxation time $\tau_J^{VT}$ accounts for collisions with all possible species of the mixture. Therefore, it is a mixture of the vibration relaxation time scales $\tau_{JI}^{VT}$ of species $J$ by exchange with the translation energy of species $I$ as

$$\frac{1}{\tau_J^{VT}} = \sum_I \frac{\gamma_I}{\tau_{JI}^{VT}}$$

where $\gamma_I$ is the mole fraction of species $I$ given by

$$\gamma_I = \frac{n_I}{n} = Y_I \frac{M}{M_I}.$$

The various relaxation times are taken from experimental data and modelled as

$$\tau_{JI}^{VT} = \alpha_{JI} \frac{T^{\beta_{JI}}}{P} \exp\left(\gamma_{JI} T^{-1/3} - \delta_{JI}\right).$$

The vibrational relaxation times for $N_2$ in O have been measured by Breshears & Bird (1968). Kiefer & Lutz's (1967) experimental data are used for the vibration times for $O_2$ in O. Both data sets have been numerically fitted by Thivet, Perrin & Candel (1991). The vibrational relaxation times for $O_2$ and $N_2$ in $N_2$ have been measured by Blackman (1955) and fitted by Treanor & Marrone (1962). In the mixture considered, oxygen and nitrogen atoms have similar masses and properties. Therefore, it is proposed to extend the available data to the other collision partners by only considering whether they are atoms or molecules.

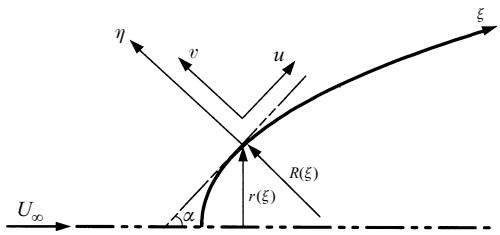


FIGURE 3. Coordinate system linked to the body surface.

### 2.5. *Thermodynamic model*

Only the three major modes, namely translation, rotation and vibration, are taken into account when modelling the partition of internal energy in the various species. Translational and rotational modes are always considered in full equilibrium and thus are characterized by a single temperature $T$, while vibrational modes may depart from equilibrium. Therefore each of the diatomic species $N_2$ and $O_2$ is assumed to have a separate vibrational temperature distinct from the mixture temperature $T$. The internal energy of each of the constituent species is calculated as the sum of the contributions of the translational and rotational energy modes, the vibrational energy modes and the heat of formation, i.e.

$$e_I = e_{trans,I} + e_{rot,I} + e_{vib,I} + h^0_{f,I}$$

where $h^0_{f,I}$ is the formation enthalpy of the species $I$, $e_{trans,I} = \frac{3}{2}(RM_I)T$ is the translation energy of a species per unit mass, $e_{rot,I} = (RM_I)T$ is the rotation energy per unit mass for a diatomic molecule. Under the assumption of an harmonic oscillator, the vibrational energy of a diatomic molecule is

$$e_{vib,I} = \frac{R\theta_{vib,I}}{M_I\left(\exp\left(\theta_{vib,I}/T_{vib,I}\right)-1\right)} - \frac{N_I R\theta_{vib,I}}{M_I\left(\exp\left(N_I\theta_{vib,I}/T_{vib,I}\right)-1\right)}$$

where $T_{vib,I}$ is the vibrational temperature of a molecule $I$, $\theta_{vib,I}$ its specific vibrational temperature and $N_I$ the number of vibration levels of the molecule. Note that for molecules in thermal equilibrium, $T$ also represents the vibrational temperature.

The internal energy of the mixture per unit mass is given by $e = \sum_I Y_I e_I$. For each species the enthalpy is $h_I = e_I + P_I/\rho_I = e_I + RT/M_I$ and the mixture enthalpy per unit mass is

$$h = \sum_I Y_I h_I = e + \frac{P}{\rho}.$$

## 3. Defect approach

### 3.1. *Dimensionless variables*

We consider a two-dimensional planar or axisymmetric flow, and we use a coordinate system linked to the body surface, where $\xi$ is the curvilinear abscissa along the body and $\eta$ is the distance along the wall normal (figure 3).

The metric coefficients are

$$h_1 = 1 + \eta/R(\xi), \quad h_3 = (r(\xi) + \eta\cos\alpha(\xi))^j$$

where $R(\xi)$ and $r(\xi)$ are respectively the longitudinal and transverse curvature radii, $\alpha(\xi)$ the angle between the wall tangent and the symmetry axis, and $j = 0$ for planar

body or $j = 1$ for axisymmetric body. The previous Navier–Stokes equations are written in dimensionless form with reference to the upstream velocity $U_\infty$, upstream density $\rho_\infty$, a reference length $R_0$ such as the nose radius, a reference temperature $T_{ref} = U_\infty^2/C_{p,f}$ and a reference viscosity $\mu_{ref}$.

### 3.2. *Dimensionless numbers of the problem*

A more convenient form of the heat flux, which will appear in the dimensionless form of the Navier–Stokes equations, is

$$\boldsymbol{\phi} = -\frac{\mu}{P_r' R_e}\left(\nabla h + \left(L_e' - 1\right)\sum_I h_I \nabla Y_I + \sum_{j=N_2,O_2}\left(F_{vib,j} - 1\right) Y_j \nabla e_{vib,j}\right)$$

with the following numbers defined as:

Reynolds number

$$R_e = \frac{\rho_\infty u_\infty L_{ref}}{\mu_{ref}};$$

Prandtl number

$$P_r' = \frac{\mu C_p'}{\lambda'};$$

where

$$\lambda' = \lambda_{trans,rot} + \lambda_{vib,NO}$$

with $\lambda_{trans,rot}$ the translation/conduction thermal conductivity, $\lambda_{vib,NO}$ the vibration thermal conductivity of NO and

$$C_p' = C_{p,trans,rot} + Y_{NO} C_{v,vib_{NO}}$$

with $C_{p,trans,rot}$ the translation/rotation specific heat of the mixture and $C_{v,vib_{NO}}$ the vibrational specific heat of NO which is assumed to be in thermal equilibrium;

Lewis number

$$L_e' = \frac{\rho D C_p'}{\lambda'}$$

which represents the ratio of the parts of the heat flux due to the energy transport by the diffusing gas mixture components and by heat conduction which depends on the transrotational temperature;

vibrational numbers

$$F_{vib,j} = \frac{\rho C_p' \lambda_{vib,j}}{\rho Y_j C_{v,vib_j} \lambda'}.$$

Under the assumption of Mason & Monchick (1962), $\lambda_{vib,j} = \rho Y_j D_{vib_j,m} C_{v,vib_j}$. Since the Fick law is used with a single diffusion coefficient, and if we assimilate the diffusion coefficient of the vibrational mode into this single diffusion coefficient, we have $D_{vib_j,m} = D$ and thus $F_{vib,j} = L_e'$. Hence the wall heat flux expression can be simplified to

$$\boldsymbol{\phi} = -\frac{\mu}{P_r' R_e}\left(\nabla h + \left(L_e' - 1\right)\sum_I h_I \nabla Y_I + \left(L_e' - 1\right)\sum_{j=N_2,O_2} Y_j \nabla e_{vib,j}\right).$$

The Schmidt number $S_c = \nu/D$ is the same in thermal non-equilibrium and at equilibrium, since we have assumed that thermal non-equilibrium does not modify the transport coefficients $\nu$ and $D$. Thus we can deduce a relation between $L_e'$, and the

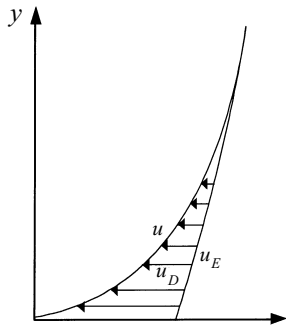


FIGURE 4. Defect velocity.

Lewis number defined at thermal equilibrium $L_e = \rho D C_{p,f}/\lambda_{eq}$, with $\lambda_{eq}$ the thermal conductivity of the mixture at thermal equilibrium, and $C_{p,f}$, the specific heat of the frozen mixture at thermal equilibrium defined by $C_{p,f} = \left(\partial h/\partial T\right)_{P,Y_I,T_{vib,I}=T} = \sum_I Y_I C_{p,I}(T)$. This relation is

$$S_c = \frac{P_r}{L_e} = \frac{P_r'}{L_e'}$$

where $P_r = \mu C_{p,f}/\lambda_{eq}$ is the Prandtl number defined at thermal equilibrium. Thus we obtain the following relation:

$$L_e' = L_e \frac{C_p'}{C_{p,f}} \frac{\lambda_{eq}}{\lambda'}$$

where the value of $L_e$ used in thermal equilibrium is taken constant and equal to 1.2.

### 3.3. *Decomposition*

According to the defect approach described in Aupoix, Brazier, & Cousteix (1992), each variable $w$ of the physical flow is split in two parts:

$$w = w_E + w_D \text{ with } w = \{u, p, \rho, h, T, \ldots\}.$$

The first part is labelled with the subscript $E$ and represents the inviscid solution which is a good approximation far from the wall. The second part, called the 'defect part' and labelled with the subscript $D$, is the difference between the viscous solution and the outer inviscid profile (figure 4) giving an approximation valid near the wall. For the normal velocity we write

$$v = v_E - v_E(\xi, 0) + v_D.$$

The term $v_E(\xi, 0)$ has been added to keep the condition $v_D(\xi, 0) = 0$ at the wall whatever the value of $v_E$. The extension to reacting flows presented here, consists in splitting the species mass fractions and the vibrational energy of $N_2$ and $O_2$ molecules, into external and defect parts, as well as the chemical production rates and the vibrational production rates:

$$\begin{aligned}
&Y_I = Y_{IE} + Y_{ID},\\
&\mathscr{E}_{vib,J} = \mathscr{E}_{vib,J,E} + \mathscr{E}_{vib,J,D} \quad \text{with} \quad \mathscr{E}_{vib,J} = Y_J e_{vib,J},\\
&\dot{\omega}_I = \dot{\omega}_{I,E} + \dot{\omega}_{I,D},\\
&\dot{\Omega}_J = \dot{\Omega}_{J,E} + \dot{\Omega}_{J,D}.
\end{aligned}$$

### 3.4. *Asymptotic expansion*

Two approximations of the Navier–Stokes equations are sought: one far from the wall, in the region where the viscous effects are weak, and the other one near the wall, where the viscous effects are important. Both solutions are defined over the whole domain but are valid only in a restricted zone. These approximations are looked for as expansions in powers of a small perturbation parameter:

$$\varepsilon = R_e^{-1/2}.$$

The external functions depend on the coordinates $(\xi, \eta)$. The outer expansions are

$$\left.\begin{aligned}
u_E(\xi,\eta) &= U_1(\xi,\eta) + \varepsilon U_2(\xi,\eta) + \cdots,\\
v_E(\xi,\eta) &= V_1(\xi,\eta) + \varepsilon V_2(\xi,\eta) + \cdots,\\
p_E(\xi,\eta) &= P_1(\xi,\eta) + \varepsilon P_2(\xi,\eta) + \cdots,\\
\rho_E(\xi,\eta) &= R_1(\xi,\eta) + \varepsilon R_2(\xi,\eta) + \cdots,\\
h_E(\xi,\eta) &= H_1(\xi,\eta) + \varepsilon H_2(\xi,\eta) + \cdots,\\
T_E(\xi,\eta) &= T_1(\xi,\eta) + \varepsilon T_2(\xi,\eta) + \cdots,\\
Y_{I,E}(\xi,\eta) &= Y_{I,1}(\xi,\eta) + \varepsilon Y_{I,2}(\xi,\eta) + \cdots,\\
\mathscr{E}_{vib,I,E}(\xi,\eta) &= \mathscr{E}_{vib,I,1}(\xi,\eta) + \varepsilon \mathscr{E}_{vib,I,2}(\xi,\eta) + \cdots,\\
T_{vib,I,E}(\xi,\eta) &= T_{vib,I,1}(\xi,\eta) + \varepsilon T_{vib,I,2}(\xi,\eta) + \cdots.
\end{aligned}\right\} \tag{3.1}$$

In the inner region, a stretched normal coordinate $\bar{\eta} = \eta/\varepsilon$ is used according to the principle of least degeneracy (Van Dyke 1962, 1975). In this way, the normal coordinate is referred to a quantity of the same order of magnitude as the boundary layer thickness, so that the new normal coordinate is of order unity in the boundary layer. Similarly, a special expansion must be written for the normal velocity because this quantity is of order $\varepsilon$ in the boundary layer, according to the continuity equation. Therefore, the inner expansions have the form

$$\left.\begin{aligned}
u_D(\xi,\eta) &= u_1(\xi,\bar{\eta}) + \varepsilon u_2(\xi,\bar{\eta}) + \cdots,\\
v_D(\xi,\eta) &= \varepsilon \bar{v}_1(\xi,\bar{\eta}) + \varepsilon^2 \bar{v}_2(\xi,\bar{\eta}) + \cdots,\\
p_D(\xi,\eta) &= p_1(\xi,\bar{\eta}) + \varepsilon p_2(\xi,\bar{\eta}) + \cdots,\\
\rho_D(\xi,\eta) &= \rho_1(\xi,\bar{\eta}) + \varepsilon \rho_2(\xi,\bar{\eta}) + \cdots,\\
h_D(\xi,\eta) &= h_1(\xi,\bar{\eta}) + \varepsilon h_2(\xi,\bar{\eta}) + \cdots,\\
T_D(\xi,\eta) &= t_1(\xi,\bar{\eta}) + \varepsilon t_2(\xi,\bar{\eta}) + \cdots,\\
Y_{I,D}(\xi,\eta) &= y_{I,1}(\xi,\bar{\eta}) + \varepsilon y_{I,2}(\xi,\bar{\eta}) + \cdots,\\
\mathscr{E}_{vib,I,D}(\xi,\eta) &= \epsilon_{vib,I,1}(\xi,\bar{\eta}) + \varepsilon \epsilon_{vib,I,2}(\xi,\bar{\eta}) + \cdots,\\
T_{vib,I,D}(\xi,\eta) &= t_{vib,I,1}(\xi,\bar{\eta}) + \varepsilon t_{vib,I,2}(\xi,\bar{\eta}) + \cdots.
\end{aligned}\right\} \tag{3.2}$$

All the coefficients and their derivatives are assumed to be of order unity. Special attention has to be paid to the order-of-magnitude analysis of the external flow quantities in the inner region. For example, the normal velocity component can be expanded as

$$V_1(\xi,\eta) - V_1(\xi,0) = \varepsilon \widetilde{V}_1(\xi,\eta).$$

### 3.5. *First-order flow equations*

In the outer region, the defect variables are null. The outer expansions are brought into the Navier–Stokes equations, and terms of like powers of $\varepsilon$ are equated. The first-order equations for the outer flow are just the usual Euler equations, as in the Van Dyke theory.

The derivation procedure for the inner-region equations is more complex. One must first bring the above expansions (3.1) and (3.2) into the Navier–Stokes equations, then

subtract the external equations, and finally equate the same powers of $\varepsilon$. For practical convenience, the inner equations can then be rewritten in outer coordinates, using $\eta$ instead of $\bar{\eta}$ and replacing $\bar{v}_1$ and $\bar{v}_2$, as

$$v_1(\xi,\eta) = \varepsilon\bar{v}_1(\xi,\bar{\eta}), \quad v_2(\xi,\eta) = \varepsilon\bar{v}_2(\xi,\bar{\eta}).$$

Like in the Van Dyke theory, $\mu$ is developed using a Taylor expansion following the relation

$$\mu(T) = \mu(T_1 + t_1 + \varepsilon(T_2 + t_2) + \cdots) = \mu(T_1 + t_1) + \varepsilon(T_2 + t_2)\frac{\mathrm{d}\mu}{\mathrm{d}T}(T_1 + t_1) + \cdots,$$

i.e.

$$\mu(T) = \mu_1 + \varepsilon\mu_2 + \cdots$$

with

$$\mu_1 = \mu(T_1 + t_1) \;\; \mu_2 = (T_2 + t_2)\frac{\mathrm{d}\mu}{\mathrm{d}T}(T_1 + t_1) + \cdots.$$

Thus we have also

$$h_{I,1} = h_I\left(T_1 + t_1, T_{vib_I,1} + t_{vib_I,1}\right) \;\; e_{vib,I,1} = e_{vib,I,1}\left(T_{vib_I,1} + t_{vib_I,1}\right).$$

Then the following first-order equations are obtained for the defect boundary layer in thermochemical non-equilibrium:

continuity

$$\frac{\partial}{\partial\xi}\left[r^j\rho_1 U_1 + r^j(R_1 + \rho_1)u_1\right] + \frac{\partial}{\partial\eta}\left[r^j\rho_1(V_1 + v_1)\right] + r^j R_1\frac{\partial v_1}{\partial\eta} = 0;$$

$\xi$- momentum

$$(R_1 + \rho_1)(U_1 + u_1)\frac{\partial u_1}{\partial\xi} + [\rho_1 U_1 + (R_1 + \rho_1)u_1]\frac{\partial U_1}{\partial\xi} + (R_1 + \rho_1)(V_1 + v_1)\frac{\partial u_1}{\partial\eta} = -\frac{\partial p_1}{\partial\xi} + \frac{1}{R_e}\frac{\partial}{\partial\eta}\left(\mu_1\frac{\partial u_1}{\partial\eta}\right);$$

$\eta$- momentum

$$0 = -\frac{\partial p_1}{\partial\eta};$$

energy

$$(R_1 + \rho_1)(U_1 + u_1)\frac{\partial h_1}{\partial\xi} + [\rho_1 U_1 + (R_1 + \rho_1)u_1]\frac{\partial H_1}{\partial\xi} + (R_1 + \rho_1)(V_1 + v_1)\frac{\partial h_1}{\partial\eta}$$
$$= u_1\frac{\partial P_1}{\partial\xi} + (U_1 + u_1)\frac{\partial p_1}{\partial\xi} + \frac{\mu_1}{R_e}\left(\frac{\partial u_1}{\partial\eta}\right)^2 + \frac{\partial}{\partial\eta}\left[\frac{\mu_1}{R_e P_r'}\frac{\partial h_1}{\partial\eta}\right]$$
$$+\frac{\partial}{\partial\eta}\left[\frac{\mu_1}{R_e P_r'}\left(\left(L_e' - 1\right)\sum_I h_{I,1}\frac{\partial y_{I,1}}{\partial\eta} + \left(L_e' - 1\right)\sum_{J=N_2,O_2}\left(\frac{\partial\epsilon_{vib,J,1}}{\partial\eta} - e_{vib,J,1}\frac{\partial y_{J,1}}{\partial\eta}\right)\right)\right];$$

species conservation

$$(R_1 + \rho_1)(U_1 + u_1)\frac{\partial y_{I,1}}{\partial\xi} + [\rho_1 U_1 + (R_1 + \rho_1)u_1]\frac{\partial Y_{I,1}}{\partial\xi} + (R_1 + \rho_1)(V_1 + v_1)\frac{\partial y_{I,1}}{\partial\eta} = \dot{\omega}_{I,D,1} + \frac{\partial}{\partial\eta}\left[\frac{\mu_1 L_e}{R_e P_r}\frac{\partial y_{I,1}}{\partial\eta}\right];$$

vibration relaxation equations

$$(R_1+\rho_1)(U_1+u_1)\frac{\partial \epsilon_{vib,J,1}}{\partial \xi}+[\rho_1 U_1+(R_1+\rho_1)u_1]\frac{\partial \mathscr{E}_{vib,J,1}}{\partial \xi}$$
$$+(R_1+\rho_1)(V_1+v_1)\frac{\partial \epsilon_{vib,J,1}}{\partial \eta}=\dot{\Omega}_{J,D,1}+\frac{\partial}{\partial \eta}\left[\frac{\mu_1 L_e}{R_e P_r}\frac{\partial \epsilon_{vib,J,1}}{\partial \eta}\right].$$

### 3.6. *Matching conditions*

Each expansion must satisfy the boundary conditions corresponding to its own domain of validity. The upstream conditions are to be applied to the outer expansion and the wall conditions to the inner one. The missing conditions are obtained by matching the inner and outer expansions. Thus at the edge of the boundary layer, the matching is obtained by letting the defect variables, except $v_D$, tend towards zero outside the boundary layer, so we can write

$$w \longrightarrow w_E \quad \text{with} \quad w=\{u,v,p,\rho,h,T,T_{vib,I},Y_I,\mathscr{E}_{vib,I}\},$$

and so for the defect variables

$$w_D \longrightarrow 0 \quad \text{with} \quad w=\{u,p,\rho,h,T,T_{vib,I},Y_I,\mathscr{E}_{vib,I}\},$$

$$v_D \longrightarrow v_E(\xi,0).$$

Thus at first order

$$\lim_{\bar{\eta}\to\infty} u_1=0, \quad \lim_{\bar{\eta}\to\infty} p_1=0, \quad \lim_{\bar{\eta}\to\infty} h_1=0, \quad \lim_{\bar{\eta}\to\infty} t_1=0,$$

$$\lim_{\bar{\eta}\to\infty} y_{I,1}=0, \quad \lim_{\bar{\eta}\to\infty} \rho_1=0, \quad \lim_{\bar{\eta}\to\infty} \epsilon_{vib,j,1}=0, \quad \lim_{\bar{\eta}\to\infty} t_{vib,j,1}=0,$$

$$V_1(\xi,0)=0.$$

Using the above condition for the pressure, the first-order $\eta$-momentum reduces to

$$p_1=0.$$

So, the pressure in the first-order boundary layer is everywhere equal to the local inviscid flow pressure, instead of its wall value as in the Van Dyke theory. The conditions on $p$, $\rho$, $Y_I$ and $T$ are not independant since they are linked through the state equation. The condition on $v$ is not a boundary condition for the inner expansion but it gives the wall condition for the outer flow. The conditions at the edge of the boundary layer ensure, even with a first-order expansion, a smooth merging of the boundary layer into the inviscid flow whatever the inviscid profiles.

### 3.7. *Wall conditions*

The wall conditions for the inner flow are

$$u=U_1+u_1+\varepsilon(U_2+u_2)=0,$$
$$v=\varepsilon\bar{v}_1+\varepsilon^2\bar{v}_2=0,$$
$$T=T_1+t_1+\varepsilon(T_2+t_2)=T_w.$$

If the wall is fully catalytic, the chemical reactions at the wall are assumed to be catalyzed at a sufficiently high rate so that the mass fractions attain local equilibrium values. Thus we have

$$Y_I=Y_{I,1}+y_{I,1}=Y_{I,eq}.$$

If the wall is non-catalytic, no chemical reaction occurs and hence there is no diffusion of any species at the wall. We obtain

$$\frac{\partial Y_I}{\partial \eta} = 0.$$

If the wall is in thermal equilibrium we have

$$T_{vib,I} = T_{vib,I,1} + t_{vib,I,1} = T_w.$$

If the wall is vibrationally non-catalytic we obtain

$$\frac{\partial T_{vib,I}}{\partial \eta} = 0,$$

i.e.

$$\frac{\partial e_{vib,I}}{\partial \eta} = 0,$$

Hence at first order the wall conditions reduce to

$u_1(\xi,0) = -U_1(\xi,0)$,

$v_1(\xi,0) = 0$,

$t_1(\xi,0) = T_w - T_1(\xi,0)$,

$y_{I,1}(\xi,0) = Y_{I,eq} - Y_{I,1}(\xi,0)$ (catalytic wall),

$\dfrac{\partial y_{I,1}}{\partial \eta}(\xi,0) = -\dfrac{\partial Y_{I,1}}{\partial \eta}(\xi,0)$ (non-catalytic wall),

$\epsilon_{vib,J,1}(\xi,0) = \left(Y_{J,1}(\xi,0) + y_{J,1}(\xi,0)\right) e_{vib,J}(T_w) - \mathscr{E}_{vib,J,1}(\xi,0)$ (wall in thermal equilibrium),

$$\frac{\partial \epsilon_{vib,J,1}}{\partial \eta}(\xi,0) - \frac{\epsilon_{vib,J,1}(\xi,0)}{Y_J(\xi,0)}\frac{\partial Y_J}{\partial \eta}(\xi,0) = -\frac{\partial \mathscr{E}_{vib,J,1}}{\partial \eta}(\xi,0) + \frac{\mathscr{E}_{vib,J,1}(\xi,0)}{Y_J(\xi,0)}\frac{\partial Y_J}{\partial \eta}(\xi,0)$$

(non catalytic vibrationally wall).

## 4. Numerical procedure

Thanks to the small-perturbations approach, the calculation of the external flow and of the boundary layer are uncoupled and are performed separately. Thus, in a first stage we solve the first-order external problem, that is the Euler equations for a thermochemically reacting flow. For solving those ten coupled equations, a second-order implicit finite difference method is implemented. This method is based on a predictor-corrector scheme. A flux splitting technique is used for the Eulerian fluxes in the implicit operator. After discretization and simplification, the block tridiagonal matrix is solved with a Gauss Seidel line relaxation method. A more detailed description of this numerical approach can be found in MacCormack (1985) and Schall, Burtschell, & Zeitoun (1995). Once we have obtained the inviscid solution, the parabolic defect boundary layer equations are solved from the stagnation line. The stagnation line equations are deduced with the help of polynomial expansions with respect to the curvilinear coordinate $\xi$, as in Van Dyke (1962). Indeed in the vicinity of the stagnation point, each variable of the outer and inner zone can be expanded in powers of $\xi$, with coefficients that are functions of $\eta$ for the outer variables, and of $\bar{\eta}$ for the defect variables. For obvious symmetry reasons we retain only the even powers of $\xi$ in each expansion except for the longitudinal velocity which depends on

| | | |
|---|---|---|
| Mach number | $\mathscr{M}_\infty$ | 14.98 |
| Velocity ($m\,s^{-1}$) | $U_\infty$ | 5612.4 |
| Density ($kg\,m^3$) | $\rho_\infty$ | $6.8714 \times 10^{-4}$ |
| Pressure (Pa) | $p_\infty$ | 71.34 |
| Temperature (K) | $T_\infty$ | 302 |
| $N_2$ vibrational temperature (K) | $Tv_{N_2\infty}$ | 5682.5 |
| $O_2$ vibrational temperature (K) | $Tv_{O_2\infty}$ | 3618.2 |
| $N_2$ mass fraction | $Y_{N_2\infty}$ | 0.784812 |
| $O_2$ mass fraction | $Y_{O_2\infty}$ | 0.002582 |
| NO mass fraction | $Y_{NO\infty}$ | 0.002812 |
| N mass fraction | $Y_{N\infty}$ | 0.003876 |
| O mass fraction | $Y_{O\infty}$ | 0.205918 |
| Reynolds number | $R_e = \dfrac{\rho_\infty u_\infty R_0}{\mu_{ref}}$ | 900 |
| Small parameter | $\varepsilon$ | 0.03333 |

TABLE 1. *ELECTRE* – F4 wind tunnel data at the nozzle exit section

the odd powers of $\xi$. Then the first-order terms of those expansions are brought in the defect equations where the $\xi$ derivatives are set to zero around the stagnation point for symmetry reasons except for the longitudinal velocity. Hence, a set of ordinary differential equations along the stagnation line is obtained, and solved iteratively after discretization. Since the first-order defect boundary layer equations are parabolic, fast space marching methods are used, like for the standard Prandtl equations, as long as the boundary layer remains attached.

The partial differential set of defect equations is discretized by using a fully implicit finite difference method for the $\eta$-direction and a two-point backward difference quotient for the $\xi$ derivatives. This finite difference method was chosen because it is easy to implement, fast, reasonably accurate, and stable. First-order spatial differences are used for the convective terms, whereas the diffusive terms are discretized by second-order differences. After discretization each defect equation can be written in tridiagonal matrix form and solved iteratively by the scalar Thomas algorithm (see for example Patankar 1980). The merging between the previously computed Euler zone, and the defect zone is achieved when the discrepancy between the inviscid solution and the viscous one tends towards zero at the edge of the defect zone.

## 5. Application to non-equilibrium hypersonic viscous flow around the *ELECTRE* model with the F4 free-stream conditions

### 5.1. *Conditions of simulation*

To apply the defect approach to hypersonic flows with real gas effects, we have performed a computational study of the high-enthalpy air flow past the blunt body *ELECTRE* defined by the ESA for the recent workshop that was held in ESTEC. The geometry is essentially a sphere–cone of nose radius $R_0 = 0.035\,m$, cone half-angle $\alpha = 4.66°$, and overall length $L = 0.4\,m$.

In this study the wall temperature is assumed to be constant with $T_w = 300\,K$. The *ELECTRE* model was selected as a standard model for reference testing in order to evaluate the high-enthalpy facility's characteristics, and also to validate CFD code in the hypervelocity flow regime. This model exhibits sufficient bluntness to produce dissociation/recombination behind the bow shock in the stagnation region.

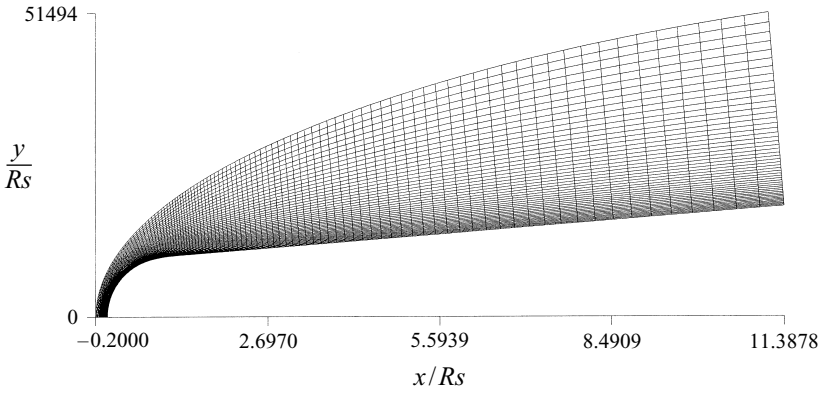


FIGURE 5. 108 × 50 grid for inviscid calculation of the flow field about *ELECTRE*.

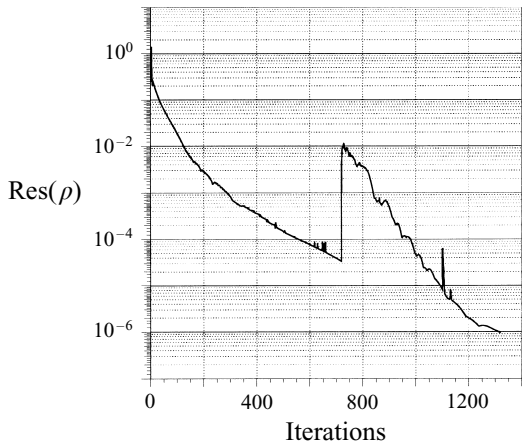


FIGURE 6. Time history convergence for L1 norm of $\rho$ residue.

The expansion from the blunt spherical part to the slender conical section might be rapid enough to display significant non-equilibrium in the expansion fan. It is a model simple enough to be transferred from tunnel to tunnel and be used to study the tunnel characteristics as they influence the non-equilibrium chemistry. The characteristics of the non-equilibrium flow at the nozzle exit of the F4 hypersonic wind tunnel, are given in table 1 of Schwane, & Muylaert (1994). Those values corresponds to a reduced total enthalpy $H_{i\infty}/RT_0 = 260$ ($T_0 = 273.15$ K and $R = 288\,\mathrm{J\,Kg^{-1}\,K^{-1}}$), and a reservoir pressure $P_{i\infty} = 430$ bar.

### 5.2. *Discussion of the results*

The purpose of this application is to compute the flow field about *ELECTRE* using the Euler/defect coupling procedure previously described. The inviscid flow solutions are obtained on a computational domain which contains (108 × 50) grid points (see figure 5) for good capturing of the gradient flow. The minimum grid spacing along the stagnation line is $\Delta\eta = 1.76 \times 10^{-5}$ m, and along the body surface it is equal to $\Delta\xi = 6.12 \times 10^{-4}$ m. The time history convergence of the normalized density residue obtained for an unsteady computation of the inviscid flow field is plotted on figure 6. The first part of this curve relates to a chemical non-equilibrium flow assumption,

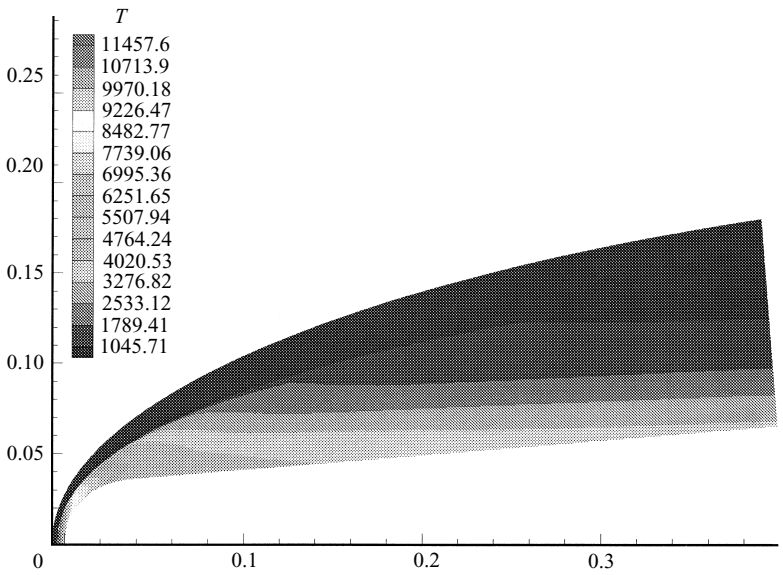


FIGURE 7. Inviscid temperature flow field on *ELECTRE*.

and the thermal non-equilibrium is added to the second part. Convergence is achieved when the residue has dropped by more than six orders of magnitude. The CPU time is about $1.10^{-3}$ s/it/pt on a Silicon Power Challenge R8000.

5.2.1. *Inviscid flow analysis*

One can see on figure 7 the inviscid temperature flow field, which has a maximum of about 11000 K behind the shock wave in the nose region.

Figure 8 demonstrates the freezing of the vibrational relaxation process for $N_2$ molecules in the expansion zone of the flow. This leads to a zone of non-constant normal gradient in the vicinity of the wall, this zone being advected on the rear part of the body. Finally, concerning the inviscid flow field, figure 9 shows the atomic oxygen mass fraction. It is interesting to observe that the Gardiner chemical model leads to a slight recombination of more than 6% of the atomic oxygen over a short distance behind the shock wave in the nose region. This phenomenon can be explained because of the exchange reactions. Indeed, since the free-stream gas flow is essentially composed of 81% of $N_2$ and 19% of O, the main reactions which occur first behind the shock wave are the $N_2$ dissociation and the second exchange reaction which leads to the NO formation. Then NO molecules react with atomic oxygen to produce $O_2$ through the first exchange reaction.

5.2.2. *Boundary layer flow analysis*

From this inviscid flow solution, the defect method is applied in order to compute the boundary layer flow on a grid of 144 points along the normal direction $\eta$. In pratice, this grid is defined by the following procedure. One first determines the maximum height for the boundary layer computational domain. To do this one considers the distance between the shock wave and the wall on the rear part of the body. Excluding the Euler grid points where the discontinuity is located, the number of points for the defect calculation grid is simply determined by a geometric progression

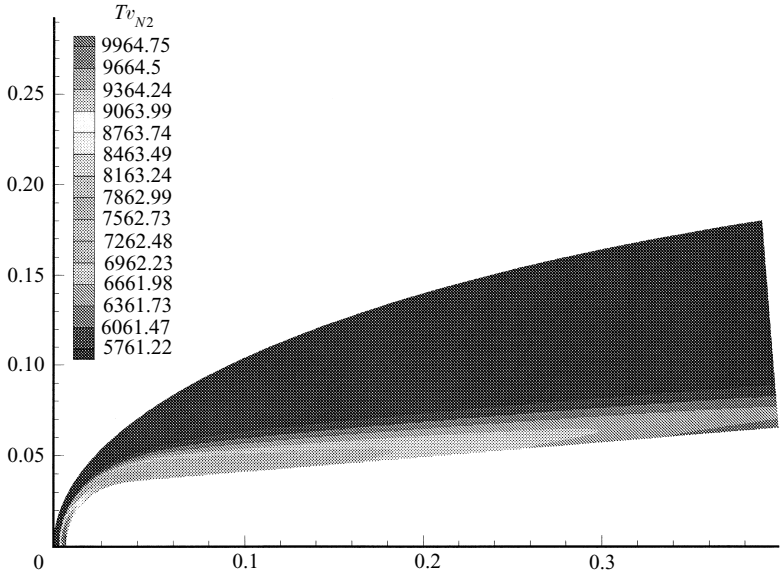


FIGURE 8. Inviscid $N_2$ vibrational temperature flow field on *ELECTRE*.

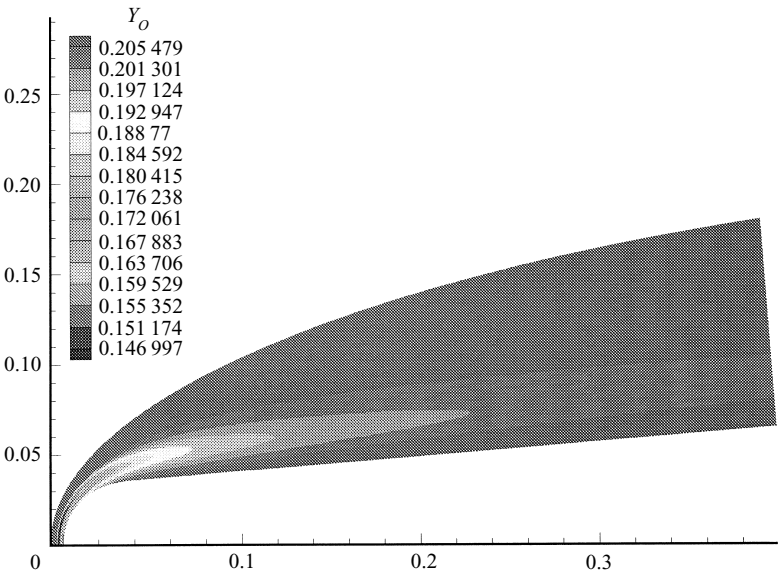


FIGURE 9. Inviscid atomic oxygen mass fraction flow field on *ELECTRE*.

based on the minimum grid spacing close to the wall and on its geometric ratio. In this study, these parameters are respectively $\Delta\eta = 1.30 \times 10^{-7}$ m and $r_\eta = 1.05$. The matching conditions between the viscous zone and the Euler one ($\bar{\eta} \to \infty$) are applied at the edge of the boundary layer computational domain, whose height is iteratively adjusted as the boundary layer grows. The additional CPU time due to the defect coupling procedure is about 10% of the Euler computation time.

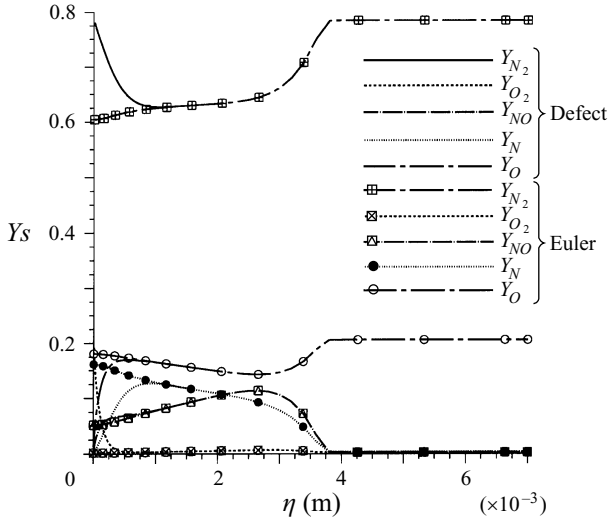


FIGURE 10. Mass fraction profiles along the stagnation streamline of *ELECTRE* – catalytic wall and $T_{vib}(0) = T_w$.

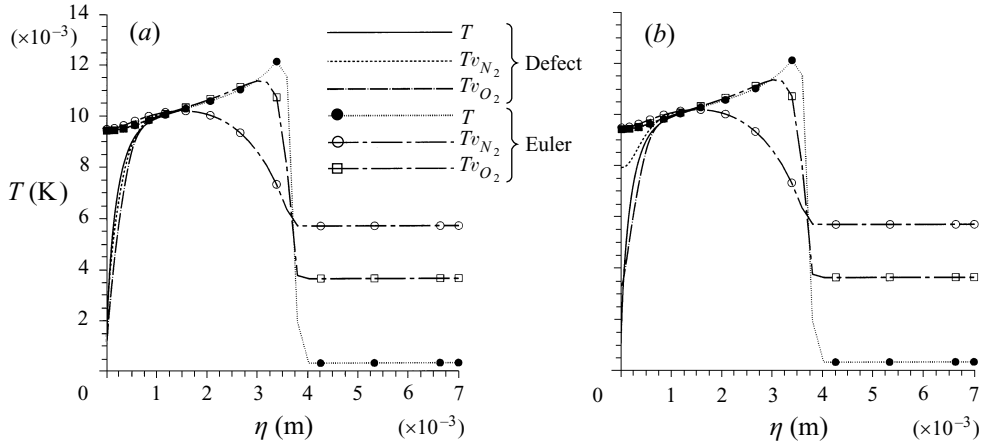


FIGURE 11. Temperature profiles along the stagnation streamline of *ELECTRE* – catalytic wall (*a*) $T_{vib}(0) = T_w$, (*b*) $q_{vib}(0) = 0$.

*A general survey of nonequilibrium processes*

Figure 10 shows the mass fraction evolution along the stagnation streamline. The level of atomic oxygen decreases behind the shock wave as previously mentioned. We can see strong recombination of atomic species in the boundary layer since we have assumed here a fully catalytic wall. Figures 11(*a*) and 11(*b*) show the evolution of the three temperatures along the stagnation streamline in the cases where a thermal equilibrium boundary condition or no vibrational energy exchanges are imposed respectively at the wall. It is interesting to notice a more pronounced thermal non-equilibrium in the boundary layer for the second case, since $Tv_{N_2}$ is about 8000 K and $Tv_{O_2}$ about 3300 K. Moreover in the outer flow the vibrational non-equilibrium region of each diatomic species is clearly visible. In the core flow the relaxation zone of $O_2$ is shorter than that of $N_2$. Figures 12(*a*) and 12(*b*) show the temperature profiles

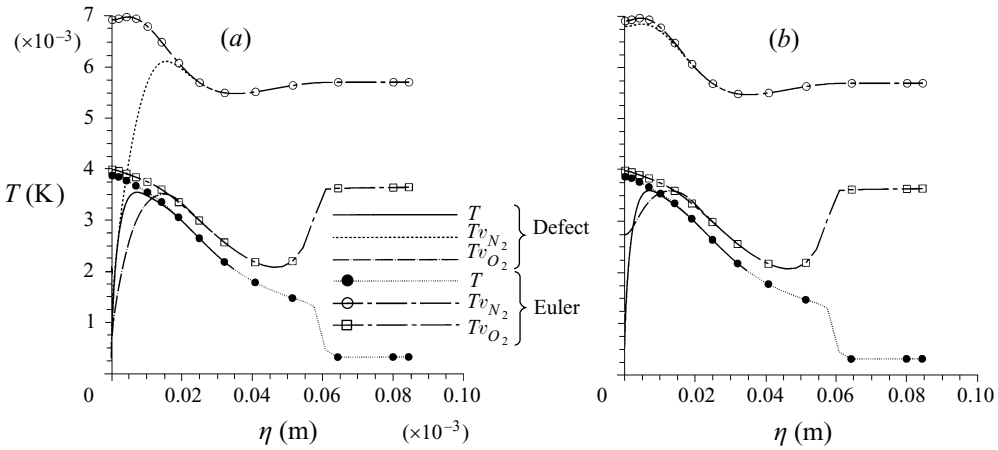


FIGURE 12. Temperature profiles at $\xi = 20$ cm – catalytic wall and (*a*) $T_{vib}(0) = T_w$, (*b*) $q_{vib}(0) = 0$.

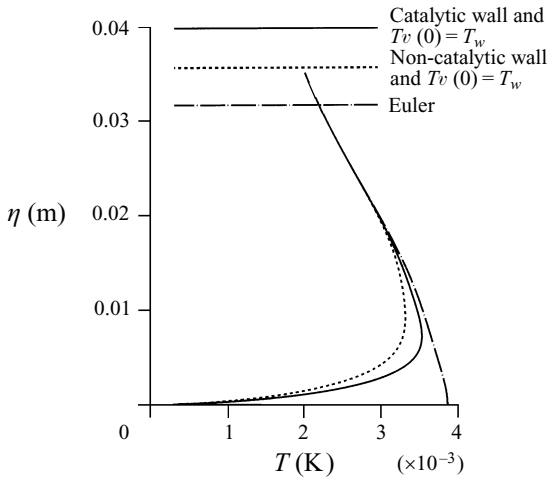


FIGURE 13. Temperature profiles in the boundary layer at $\xi = 20$ cm.

at a distance of 20 cm from the stagnation point for the two extreme boundary conditions used for the vibrational mode. One can see on these figures the freezing of the vibrational relaxation process in the expansion zone, and interestingly that the boundary layer thickness for the vibrational temperatures is larger than for the transrotational temperature.

*Thermochemical wall boundary conditions and heat flux predictions*

The influence of the catalycity at the wall on temperature profiles can be seen on figure 13. In the case of a catalytic wall, the atomic recombination is very important near the wall while molecule dissociation is very weak. Since the recombination reactions are essentially exothermic, the temperature profile is higher than in the case of a non-catalytic wall. Thus the temperature gradient at the wall is greater for a catalytic wall and consequently the wall heat flux will be increased.

The influence of the wall catalycity on the vibrational temperature profiles can be seen on figures 14(*a*) to 14(*d*). It appears that when the wall is assumed to be in thermal equilibrium, the chemical catalycity of the wall does not modify the $N_2$ vibrational

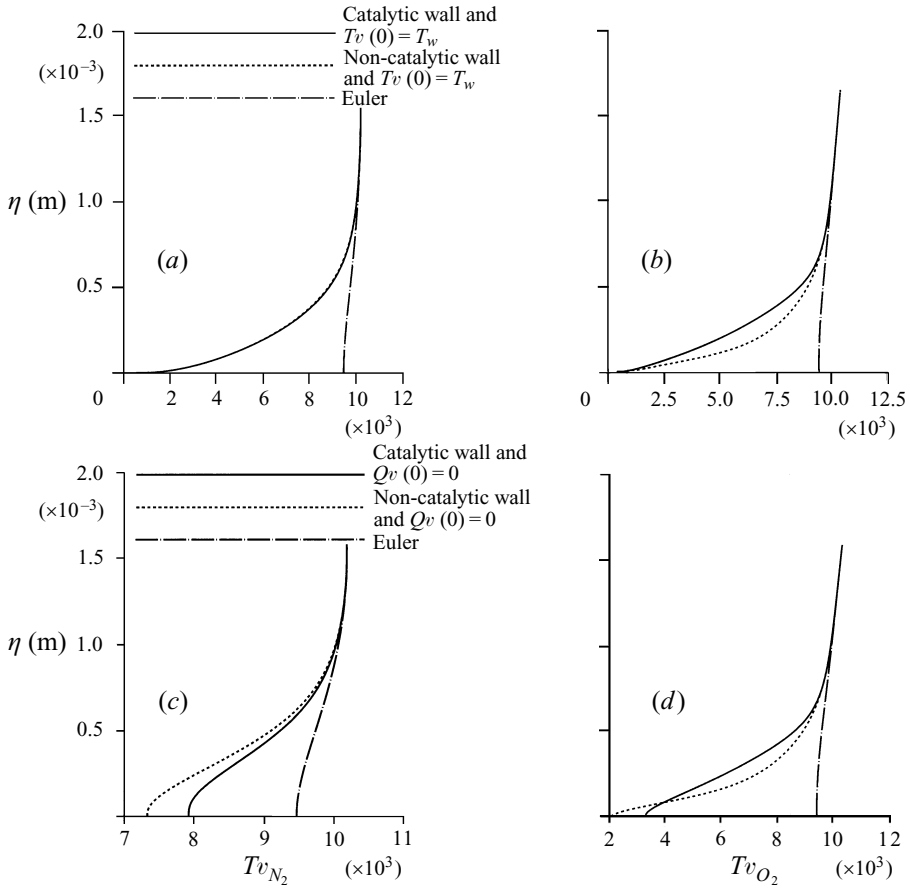


FIGURE 14. (*a*) $N_2$ and (*b*) $O_2$ vibrational temperature profiles in the boundary layer at $\xi = 0$ cm – $T_{vib}(0) = T_w$. (*c*) $N_2$ and (*d*) $O_2$ vibrational temperature profiles in the boundary layer at $\xi = 0$ cm – $q_{vib}(0) = 0$.

temperature profile (figure 14*a*), whereas $O_2$ molecules (figure 14*b*) seem to be more sensitive since in the case of a catalytic wall the $O_2$ vibrational temperature is lower than that obtained with a non-catalytic wall. This result demonstrates a transfer from the vibrational mode of oxygen molecules to the translation/rotation mode during the recombination of the atomic oxygen, which increases the temperature $T$ in the boundary layer (see figure 13). Consequently, atomic oxygen recombination which occurs in the boundary layer has lowered the mean vibrational energy of oxygen molecules.

When there is no vibrational energy exchange at the wall, the chemical catalycity of the wall has more influence on the $N_2$ vibrational temperature (figure 14*c*), since with a chemical catalytic wall the mean vibrational energy of $N_2$ molecules is increased. The same conclusions are true for the $O_2$ molecules only very close to the wall (figure 14*d*) since in the upper part of the boundary layer we observed an inversion of the behaviour. Figure 15 shows the computational wall heat transfer distribution along the *ELECTRE* model, for either a fully catalytic or non-catalytic assumption with either a full accommodation of the vibrational mode of excited molecules at the wall, or no vibrational energy exchanges at the wall. The catalytic effect produces discrepancies in the heat flux due to the diffusive contribution $\sum_I h_I \boldsymbol{Q}^D_{vib,I}$. This contribution is zero

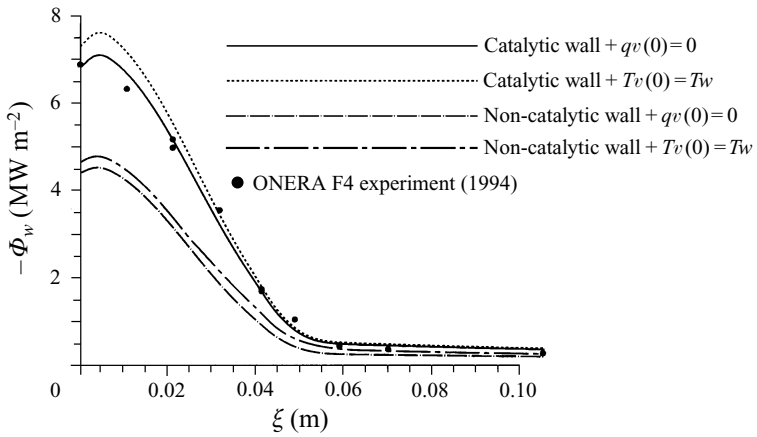


FIGURE 15. Wall heat flux predictions for the various boundary conditions.

for the 'non-catalytic' model, that gives the minimum heat flux. The recombination of atomic species via exothermal reactions liberates energy that is carried away by the surface. The 'fully catalytic' heat flux is the largest (30% higher than the 'non-catalytic') according to the maximum recombination of oxygen close to the wall (the atomic nitrogen mass fraction is negligible). The influence of the boundary condition used for the vibrational energy on the total heat flux is clearly visible. For a catalytic wall the assumption of a full accomodation of the vibrational mode of the $N_2$ and $O_2$ molecules at the wall induces a nose heat flux 13 % higher than for a wall without vibrational energy exchanges. For a non-catalytic wall the deviation in the nose heat flux between these two extreme conditions is 10%. These results confirm the previous one obtained by Tirsky (1993) concerning wall heat flux predictions for the Buran shuttle. One can observe on figure 15 that a better agreement with the experiment is achieved when the simulation takes into account a fully catalytic wall with no vibrational energy exchange at the wall. This trend is particularly true in the compression zone. Indeed, it seems that for a better comparison to experiment and for accurate predictions of the heat flux, it is required to model the partial catalycity of the wall with finite-rate catalytic boundary conditions as explained by Scott (1984), since on the rear part of *ELECTRE*, the experimental measurements are located between the two extremes of catalytic or non-catalytic behaviours. Although they strongly modify the heat flux prediction, those various boundary conditions do not influence the skin friction plotted on figure 16. In the compression zone the influence of the normal gradients is clearly evident, since with the defect approach a noticeable increase is obtained. The classical boundary layer theory overestimates the skin friction on the rear part of the body, since past the compression zone the longitudinal velocity gradient at the wall is higher than using the defect approach. The reason of such a behaviour can be found in the overestimation of the inviscid longitudinal velocity at the wall given by all the Euler solvers for reacting flows as has been shown in Désidéri & Salvetti (1993).

### 5.2.3. *Comparison with a Navier–Stokes solution*

In order to validate the coupled Euler/defect approach, a comparison with the full Navier–Stokes one has been carried out at a distance equal to 11 cm along the body. The Navier–Stokes code is an extension of the Euler one by the addition of the viscous terms in the equations, and a detailed description can be found in

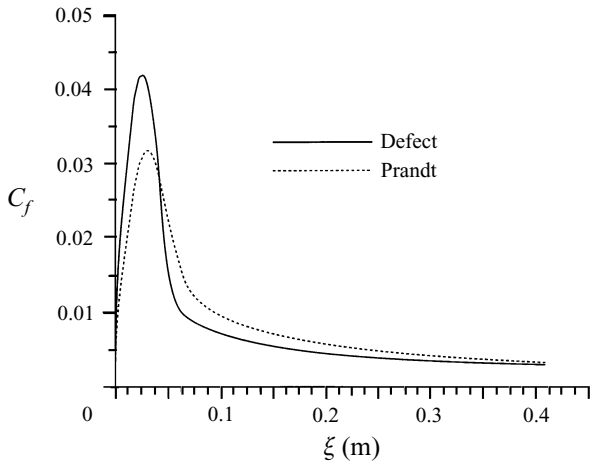


FIGURE 16. Skin friction predictions.

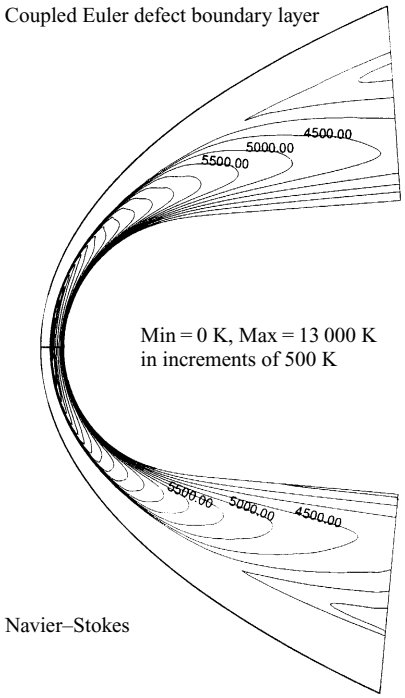


FIGURE 17. Contour plots of $Tv_{O_2}$ vibrational temperature.

MacCormack (1985) and Schall *et al.* (1995). This point is of importance since to minimize the discrepancies that can occur between the Euler and Navier–Stokes solvers, in the computation of the non-viscous region of the shock layer, one must use a similar numerical approach, and also the same physico-chemical models. The wall is assumed to be fully catalytic and there is no vibrational energy exchange at the wall. The CPU time for obtaining the steady Navier–Stokes solution is about one order of magnitude greater than the Euler one, and this easily explains the interest of the defect approach. An isocontour plot of the vibrational temperature of oxygen molecules is

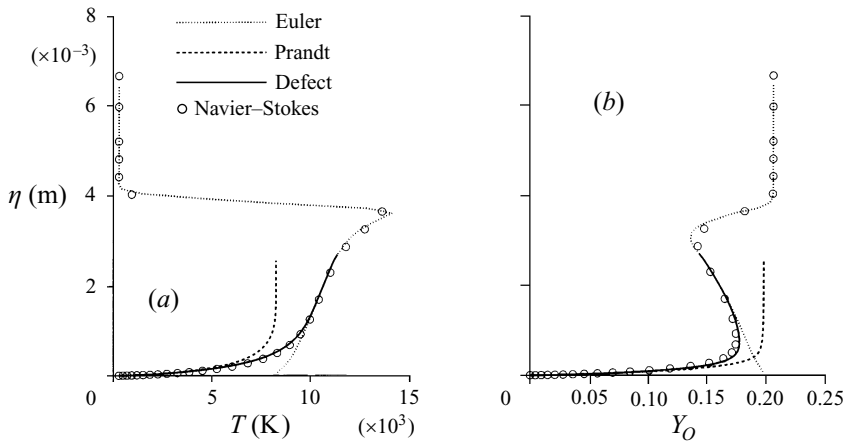


FIGURE 18. (*a*) Temperature and (*b*) atomic oxygen mass fraction profiles along the stagnation line – catalytic wall and $q_{vib}(0) = 0$.

shown on figure 17. The upper part represents the Euler/defect boundary layer solution, while the Navier–Stokes one is shown in the lower part. The two solutions are very similar. Some profiles at the stagnation point are displayed on figures 18(*a*) and 18(*b*) respectively for the temperature and the atomic oxygen mass fraction. The solution is plotted in the full computation domain in order to see the relative position of the viscous zone in the shock layer. The defect solution is very close to the Navier–Stokes one. The thermal boundary layer region occupies about 15% of the shock layer. Moreover, since we have used a very similar mesh distribution near the shock position, the result is that the shock stand-off positions given by the two solver are much the same. It should be noted that the inviscid flow gradients at the wall are non-negligible. For example, concerning the inviscid temperature $T$, the gradient decreases between the wall and the boundary layer edge. So, even with a second-order expansion, the Van Dyke method could not give a good matching, since it considers only the wall value of the gradient. In such a case, the nose heat flux would have been overestimated. The comparison is also done in the expansion zone of the flow at 11 cm from the nose. The longitudinal velocity boundary layer profile is plotted on figure 19(*a*). Here again the defect and Navier–Stokes solutions are in a good agreement. Because of the conservation of the total enthalpy in the absence of viscous effects, the positive velocity gradient at the wall for the inviscid solution induces a negative enthalpy gradient at the wall for the inviscid enthalpy profile (see figure 19*b*). As a consequence, the wall heat flux given by the defect approach is lower than the Prandtl prediction at this location as can be seen on figure 20, and the defect/Navier–Stokes comparison (figure 19*b*) exhibits some differences for the enthalpy profile. Finally the molecular oxygen mass fraction profile is plotted on figure 19(*c*), and confirms that the defect approach greatly improves the prediction of the flow field compared to the classical boundary layer theory the full Navier–Stokes solution.

The wall heat flux distributions obtained by these differents numerical approaches, to which we add a PNS solution given by Hachemin & Vérant (1995), are plotted on figure 20. Compared to the classical approach referred to as Prandtl, it is clear that the defect theory extended to real gas flow greatly improves the wall heat flux prediction. Moreover, very near the nose, the defect solution seems closer to the PNS one than the Navier–Stokes solution, which predict a nose heat flux slightly higher.

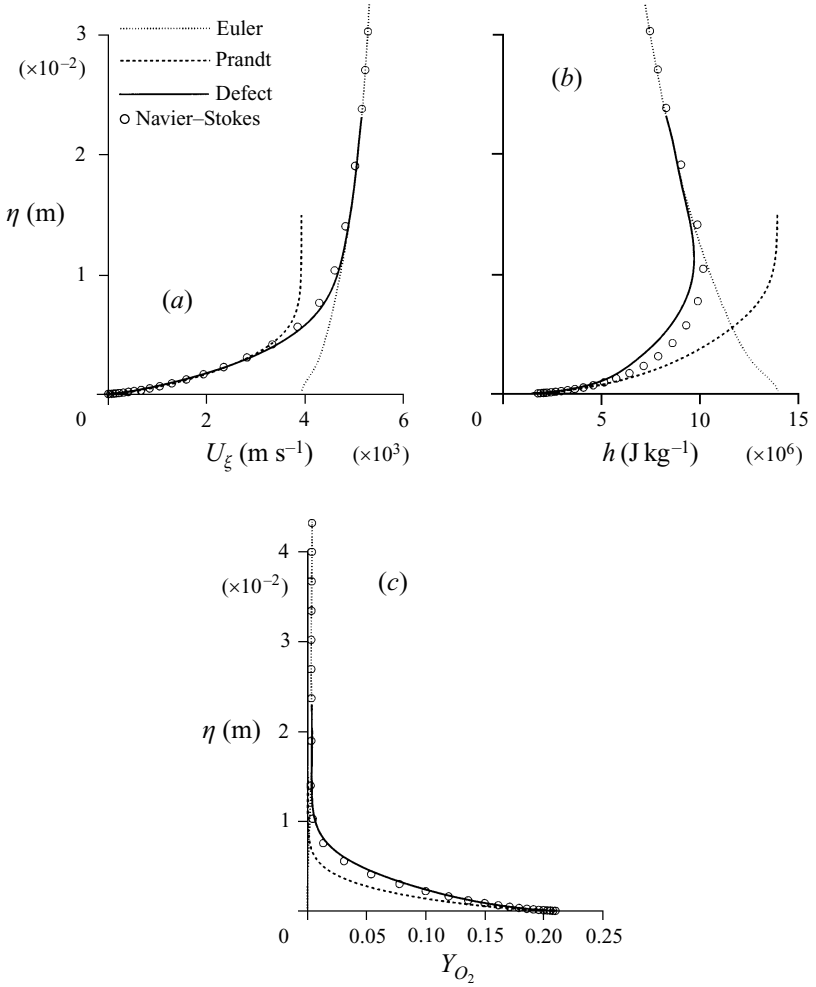


FIGURE 19. (*a*) Longitudinal velocity and (*b*) enthalpy profiles at $\xi = 11$ cm – catalytic wall and $q_{vib}(0) = 0$. (*c*) Oxygen mass fraction profiles at $\xi = 11$ cm.

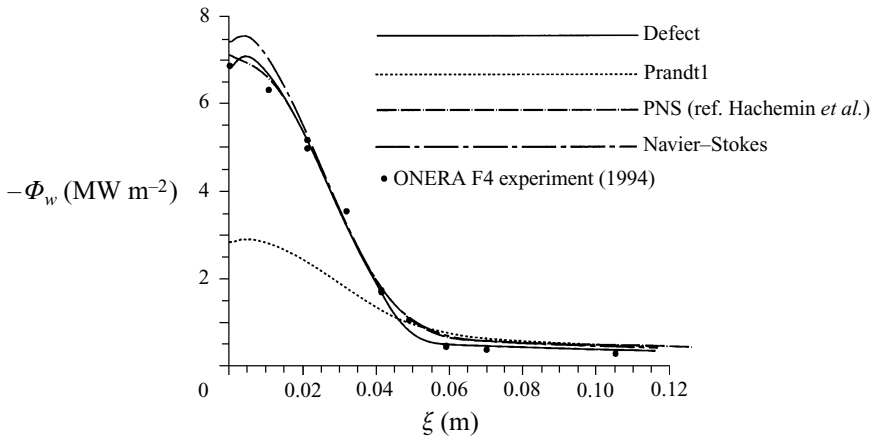


FIGURE 20. Comparison between the defect approach, the Prandtl solution, a PNS computation, a full Navier–Stokes solution and the experimental data for the wall heat flux.

The difference does not exceed 6%. It is interesting to observe the convergence of the three numerical solutions in the compression zone along the *ELECTRE* body, between 2 cm and 4 cm. The PNS method recasts exactly the full Navier–Stokes one on the rear part, where the two methods overestimate slightly the wall heat flux compared to the experimental data, whereas the defect prediction is in a better agreement with experience. Those differences, even though they are not so important, may be explained through the numerical diffusive nature of the Navier–Stokes and PNS solvers, in which artificial viscosity terms are used through an adaptative dissipation technique for preventing oscillations of the numerical scheme, as it is detailed in Jameson, Schmidt, & Turkel (1981). In addition, even though the prediction given by the defect approach is closer to the experimental data, any comparison to experimental measurements must be done carefully in view of uncertainties concerning first the thermochemical wall boundary conditions, and secondly the effective total enthalpy in the chamber of the F4 facility during the run as shown in Bellucci *et al.* (1995).

## 6. Conclusions

The defect approach has been extended to derive boundary layer equations from the Navier–Stokes equations for laminar viscous flows in thermochemical non-equilibrium. Together with matched asymptotic expansions methodology, it ensures a correct matching of the inviscid flow with the first-order boundary layer solution. The defect equations are solved for a cost similar to the standard boundary layer ones, since the problem is again parabolic. The computational prediction of the flow around the *ELECTRE* model tested in the F4 high-enthalpy wind tunnel facility has been done and catalytic effects have shown as well as the vibrational behaviour at the wall. Given identical physical, chemical and vibrational models, the comparative study between the defect boundary layer approach and the full Navier–Stokes one has showed that our method can provide a quite comparable flow solution with an important reduction of computational cost. Indeed, one can affirm, in order to give a very crude estimate, that the computational cost diminishes about in the ratio of the CPU time required between an Euler solver to a full Navier–Stokes one. Wall heat flux predictions for various boundary conditions have shown that the best agreement with the experimental data is achieved for a fully catalytic wall assuming that there is no vibrational energy exchanges at the wall. The defect boundary layer approach extended to real gas flows is a very powerful tool which will allow us to test more easily the influence on the wall heat flux of different wall boundary conditions, multicomponent diffusion models, or non-equilibrium vibrational models taking into account the various couplings between the chemistry and the vibrational energy.

The authors would like to thank the "Centre de Calcul Haute Performance de l'IRPHE Marseille" for allowing them access to the Powerchallenge Silicon R8000 computer.

## REFERENCES

Aupoix, B., Brazier, J.-Ph. & Cousteix, J. 1992 Asymptotic defect boundary-layer theory applied to hypersonic flows. *AIAA J.* **30**, 1252–1259.

Barrère, M. & Prudhomme, R. 1973 *Equations Fondamentales de l'Aérothermochimie.* Masson et Cie.

Bellucci, V., Ueda, S., Eitelberg, G. & Muylaert, J. 1995 Experimental and numerical analysis of a blunt body configuration in T5 and HEG. In *Proc. Second European Symp. on Aerothermo-*

*dynamics for Space Vehicles* (ed. J. J. Hunt). ESA SP-367 ESA Publications Division, ESTEC, Noordwijk, The Netherlands.

Blackman, V. 1955 Vibrational relaxation in oxygen and nitrogen. *Tech. Rep., Palmer Physics Laboratory, Princeton University*.

Brazier, J.Ph., Aupoix, B. & Cousteix, J. 1990 Etude asymptotique de la couche limite en formulation déficitaire. *CR Acad. Sci. Paris* (II) **310**, 1583–1588.

Breashears, W. D. & Bird, P. F. 1968 Effects of oxygen atoms on the vibrational relaxation of nitrogen. *J. Chem. Phys.* **48**, 4773.

Désidéri, J. A. & Salvetti, M. V. 1993 Inviscid non-equilibrium flow in the vincinity of a stagnation point. *CR Acad. Sci. Paris* (I) **316**, 525–530.

Gardiner, W. C. 1984 *Combustion Chemistry*. Springer-Verlag.

Glotz, G. & Schönauer, W. 1977 Einflu$\beta$ des Chemiemodells und der Randbedingungen auf die Hyperschallgrenzschicht bei Luft. Universität Karlsruhe - Rechenzentrum interner Bericht No.12.

Hachemin, J. V. & Vérant, J. L. 1995 3D parallel multiblocks thermo-chemical nonequilibrium simulation with a PNS solver. In *Proc. Second European Symp. on Aerothermodynamics for Space Vehicles* (ed. J. J. Hunt). ESA SP-367 ESA Publications Division, ESTEC, Noordwijk, The Netherlands.

Hattikudur, U. R. & Thodos, G. 1970 Equations for the collisions integrals $\Omega^{(1,1)*}$ and $\Omega^{(2,2)*}$. *J. Chem. Phys.* **52**, 4313.

Hirschfelder, J. O., Curtiss, C. F. & Bird, R. B. 1954 *Molecular Theory of Gases and Liquids*. John Wiley and Sons.

Jameson, A., Schmidt, W. & Turkel, E. 1981 Numerical solutions of the Euler equations by finite volume methods using Runge-Kutta time stepping schemes. *AIAA Paper* 81-1259.

Kiefer, J. H. & Lutz, R. W. 1967 The effect of oxygen atoms on the vibrational relaxation of oxygen. In *Proc. 11th Symp. on Combustion*, pp. 67–74, Pittsburg.

Landau, L. & Teller, E. 1936 Theory of sound dispersion. *Phys. Z. Sowjetunion* **10**, 34–43.

MacCormack, R. W. 1985 Current status of numerical solutions of the Navier–Stokes equations. *AIAA Paper* 85-0032.

Mason, E. A. & Monchick, L. 1962 Heat conductivity of polyatomic and polar gases. *J. Chem. Phys.* **36**, 1622–1640.

Pascal, S. & Brun, R. 1993 Transport properties of nonequilibrium gas mixtures. *Phys. Rev.* E **47**, 3251–3267.

Patankar, S. V. 1980 *Numerical Heat Transfer and Fluid Flow*. Series in Computational Methods in Mechanics and Thermal Sciences. McGraw Hill.

Schall, E., Burtschell, Y. & Zeitoun, D. E. 1995 Numerical study of non-equilibrium processes in high enthalpy flows. *Intl J. Numer. Meth. Heat Fluid Flow* **5**, 271–281.

Schwane, R. & Muylaert, J. 1994 Description of test cases. *Fourth European High Velocities Database Workshop*. ESTEC document YPA/1495/RS Noordwijk.

Scott, C. D. 1984 The effects of thermochemistry, nonequilibrium, and surface catalysis in the design of hypersonic vehicles. In *1st Joint Europe-US Short Course on Hypersonics*. GAMNI-SMAI.

Thivet, F., Perrin, M. Y. & Candel, S. 1991 A unified nonequilibrium model for hypersonic flows. *Phys. Fluids* A **3**, 2799–2812.

Tirsky, G. A. 1993 Up to date gasdynamic models of hypersonic aerodynamics and heat transfer with real gas properties. *Ann. Rev. Fluid Mech.* **25**, 151–181.

Treanor, C. E. & Marrone, P. V. 1962 Effects of dissociation on the rate of vibrational relaxation. *Phys. Fluids* **5**, 1022–1026.

Van Dyke, M. 1962 Second order compressible boundary layer theory with application to blunt bodies in hypersonic flow. In *Hypersonic Flow Research* (ed. F. R. Ridell), vol. 7, pp. 37–76. Academic Press.

Van Dyke, M. 1975 *Perturbation Methods in Fluid Mechanics*. The Parabolic Press, Stanford, California.

Wilke, C. R. 1950 A viscosity equation for gas mixtures. *J. Chem. Phys.* **18**, 517–519.

Wüthrich, S. & Sawley, M. L. 1992 Coupled Euler/boundary layer method for non-equilibrium, chemically reacting hypersonic flows. *AIAA J.* **30**, 2836–2844.

Zeitoun, D. E., Schall, E., Burtschell, Y. & Druguet, M. C. 1995 Vibration-dissociation coupling in nonequilibrium hypersonic viscous flows. *AIAA J.* **33**, 79–85.